ORIGINAL PAPER

Visible light-induced photocatalytic and antibacterial activity of TiO$_2$/polyaniline-kapok fiber nanocomposite

Rontgen B. Gapusan[1] · Mary Donnabelle L. Balela[1] (ID)

© The Author(s), under exclusive licence to Springer-Verlag GmbH Germany, part of Springer Nature 2021

Abstract

Anatase TiO$_2$ nanoparticles with an average crystallite size of around 6.06 nm were successfully immobilized on the surface of polyaniline-coated kapok fiber (PANI-KpF) via hydrothermal reaction. The photocatalytic activity of the TiO$_2$/PANI-KpF nanocomposite was studied under visible light using methyl orange (MO) and Cr(VI) as model pollutants. Photodegradation of MO was achieved using nanocomposites prepared with 0.5 and 1.0 mL titanium isopropoxide (TTIP) with removal efficiencies of about 87.4 and 76.8%, respectively. These are about 13 and 18% higher than the removal efficiencies under dark conditions. On the other hand, visible light-induced photo-reduction of Cr(VI) was carried out in the presence of isopropanol (IPA) as a hole scavenger, with 100% removal efficiency. Without IPA, Cr(VI) was removed by adsorption. The TiO$_2$/PANI-KpF also showed antibacterial activity against *E. coli* bacteria under visible light.

Keywords Kapok fiber · Polyaniline · Anatase TiO$_2$ · Photocatalysis · Antibacterial

Introduction

Heterogeneous photocatalysis, also known as advanced oxidation process (AOP), has been proven to be an efficient technology for degrading or transforming a wide variety of organic and inorganic pollutants into less harmful substances via oxidative or reductive mechanisms [1, 2]. This process involves the activation of a photocatalyst, typically a semiconductor material, by an incident photon with an energy (hv) equivalent or greater than its bandgap (E_G), producing energetic electron–hole pair. Anatase titanium dioxide (TiO$_2$) has been one of the most extensively investigated photocatalysts for carbon dioxide and solar energy conversion, water splitting, and

---

✉ Mary Donnabelle L. Balela
mlbalela1@up.edu.ph

1   Sustainable Electronic Materials Group, Department of Mining, Metallurgical, and Materials Engineering, College of Engineering, University of the Philippines Diliman, 1101 Quezon City, Philippines

photodegradation in both gaseous and aqueous systems [1–5]. This is due to its high photocatalytic activity, excellent chemical and thermal stabilities, long-term photostability, low-cost synthesis, and non-toxicity. However, due to its wide bandgap (3.2 eV), anatase TiO_2 can only be activated by UV light, which occupies only about 3–5% of the solar spectrum [3, 4, 6]. This limits its use under solar illumination.

Different approaches have been employed to extend the absorption of TiO_2 in the visible light region and improve its activity under sunlight. These include doping with transition metals (e.g., Mn, Fe, Co, Ni, and Bi) [7, 8], noble metals (e.g., Pd, Pt, Au, and Ag) [9, 10], and non-metals (e.g., B, C, N, S, and I) [11–13], dye sensitization [14, 15], and coupling with narrow bandgap semiconductors [16, 17]. Photosensitization using organic dyes as sensitizers has been extensively applied to improve the photocatalytic activity of TiO_2, especially in solar cell applications [18–21]. Upon solar illumination, the adsorbed dye molecule on the surface of TiO_2 gets excited and subsequently donates electrons to the conduction band of the semiconductor [22]. This would lead to the efficient separation of charges at the TiO_2 and dye sensitizer interface. Conducting polymers, such as polyaniline (PANI) and polypyrrole (PPy), could also act as photosensitizers when coupled with TiO_2 [6, 23, 24].

PANI is regarded as one of the most promising members of the intrinsically conductive polymers (ICPs) because of its tunable structure and electronic property, high environmental stability, low-cost monomer, and ease of synthesis [25, 26]. With a bandgap in the range of 1.3–2.7 eV, PANI exhibits strong absorption for visible light, making it a potential photosensitizer for TiO_2 [27]. Since the conduction band edge of PANI is more negative than that of TiO_2, the photoexcited electrons in the PANI conduction band could easily migrate to the conduction band of TiO_2 when illuminated with visible light. Consequently, the electron density in the TiO_2 conduction band increases [28]. Moreover, the photoexcited holes are trapped in the valence band of PANI, which inhibits charge recombination. In addition to the enhanced photocatalytic activity under sunlight, the amine and imine functional groups in the PANI backbone would serve as adsorption sites for heavy metals and other polar pollutants [29–33]. This would increase the concentration of pollutants in the proximity of the photoactive surface of TiO_2.

Since photocatalysis is a surface and interface process, the photocatalytic activity of TiO_2 increases with increasing surface area [13, 34, 35]. This lead to the synthesis of TiO_2 nanoparticles. Techniques such as hydrothermal process, sol–gel process, electrodeposition, solvothermal, and chemical vapor depositions have been employed in preparing TiO_2 nanoparticles [36–40]. The hydrothermal method, a simple and environmentally friendly synthesis technique, produces TiO_2 nanoparticles with a high degree of crystallinity, homogeneity in composition, and desired size and morphology [41, 42]. It typically involves the heat treatment of the one-pot mixture of the titanium precursor (e.g., titanium isopropoxide, titanium-ethoxide, tetrabutyl titanate, TiO_2 powder), ethanol, and water together with the substrate material in a Teflon-lined stainless steel autoclave at a temperature range of 60–200 °C for at least 12 h [36, 41–44].

The immobilization of photocatalysts on a carrier or support is also a convenient approach to facilitate their recovery after use. Natural fibers, such as kenaf, jute,

sisal, cotton, and kapok, have been utilized as a support for the preparation of various composite materials due to their abundance, renewability, and low cost [30–33, 45–51]. Among these natural fibers, kapok fiber (*Ceiba pentandra* L. Gaertn.) is promising because of its high surface-area-to-volume ratio owing to its hollow microtubular structure [52, 53]. Kapok fibers are mostly cultivated in Southeast Asia, East Asia, Africa, and South America and are traditionally used as stuffing material for bedding, upholstery, and life preservers due to their light-weight and high buoyancy [54, 55]. Recently, kapok fibers have been used as support for the synthesis of various polymer films, such as PPy, PANI, and polyacrylonitrile (PAN), with controllable thickness and morphology [30–33, 45, 46, 51, 56, 57]. Because of the high surface roughness and specific surface area of the resulting composites, these polymer-coated kapok fibers were utilized as a carrier for the immobilization of various catalyst nanoparticles [33, 45, 57].

The present study reports the preparation of TiO_2/PANI-coated kapok fiber (TiO_2/PANI-KpF) nanocomposite for the visible light-activated photodegradation of methyl orange (MO) and photo-reduction of chromium(VI) [Cr(VI)] in an aqueous solution. First, PANI-coated kapok fiber (PANI-KpF) was synthesized via in situ polymerization of aniline monomer on the surface of kapok fibers in an acidic solution using ammonium persulfate (APS) as the oxidizing agent. The immobilization of TiO_2 nanoparticles on the surface of PANI-KpF was carried out via a hydrothermal method using titanium isopropoxide (TTIP) as the Ti source. The effect of initial TTIP concentration on the amount of immobilized TiO_2 nanoparticles on the surface of PANI-KpF was investigated by field-emission scanning electron microscopy (FE-SEM) and energy-dispersive X-ray spectroscopy (EDX). Further, its effect on the photocatalytic activity of the TiO_2/PANI-KpF nanocomposites for the degradation of MO and reduction in Cr(VI) under visible light was evaluated. The effect of visible light irradiation on the antibacterial activity of the TiO_2/PANI-KpF nanocomposite was also investigated using *Escherichia coli* (*E. coli*) as the test microorganism.

Methodology

Pre-treatment of kapok fibers

The kapok fibers were obtained from the University of the Philippines Los Baños, Laguna during the maturation of its seed pod. After manually isolating from the kapok seeds, the fibers were treated with sodium chlorite ($NaClO_2$, 80%, Sigma-Aldrich) to remove its lignin content [32, 58]. The $NaClO_2$-solution was prepared by dissolving 1.0 g $NaClO_2$ in 100 mL distilled water while adding 1.5 mL glacial acetic acid (HOAc or CH_3COOH, 99.9%, Duksan). The treatment was performed by reacting 1.5 g kapok fibers with the $NaClO_2$-solution at 90 °C for 1 h. Upon completing the treatment, the kapok fibers were washed several times with distilled water and finally rinsed with 96% ethanol. The fibers were dried in an oven at 80 °C for 10 h.

Synthesis of PANI-coated kapok fiber nanocomposite

The deposition of PANI on the surface of $NaClO_2$-treated kapok fiber was carried out via in situ oxidative polymerization of aniline/anilinium monomer on the surface of the fiber in acidic solution using ammonium persulfate or APS ([NH_4]$_2$$S_2$$O_8$, 97.5%, Himedia) as oxidizing agent [30, 32]. Anilinium solution was prepared by dissolving 1.0 mL aniline monomer ($C_6H_5NH_2$, 99.5%, Loba Chemie) in 50 mL 1.0 M hydrochloric acid (HCl, 37% wt., Macron). Afterward, 400 mg $NaClO_2$-treated kapok fiber ($NaClO_2$-KpF) was added into the solution and stirred. The mixture was then transferred to an ice bath with continuous stirring. Meanwhile, an APS solution was prepared by dissolving 3.5 g of APS in 10 mL 1.0 M HCl. The polymerization was initiated by the dropwise addition of the pre-cooled APS solution into the kapok-anilinium mixture. The mixture was stirred continuously for 1 h while in an ice bath and allowed to complete the reaction for 16 h at room temperature. Finally, the PANI-coated KpF (PANI-KpF) nanocomposites were thoroughly washed with distilled water and subsequently rinsed with 96% EtOH before drying at 80 °C for 10 h.

Immobilization of TiO_2 nanoparticles on PANI-KpF nanocomposite

The immobilization of TiO_2 nanoparticles on the PANI-KpF was done via hydrothermal reaction process [47]. First, 400 mg PANI-KpF was dispersed in a solution containing 25 mL absolute EtOH and 25 mL distilled water via magnetic stirring. In a separate solution, 0.5–2.0 mL titanium isopropoxide or TTIP {Ti[OCH($CH3$)$_2$]$_4$, 97%, Sigma-Aldrich} was dissolved in 25 mL absolute EtOH. The TTIP solution was added dropwise into the PANI-KpF and ethanol mixture while being stirred. The resulting mixture was then continuously stirred for 1 h at room temperature. Afterward, it was transferred into a Teflon-lined stainless steel autoclave reactor and allowed to react at 80 °C for 24 h. After cooling down to room temperature, the resulting product was washed with distilled water and 96% EtOH before drying at 80 °C. Additionally, a similar hydrothermal method was carried out in the absence of PANI-KpF to synthesize pure TiO_2 nanoparticles.

Material characterizations

Morphological and microstructural investigations were performed using a field-emission scanning electron microscope (FE-SEM, Hitachi SU8230) and a field-emission transmission electron microscope (FE-TEM, JEOL JEM-2100F), respectively. Elemental analysis was carried out using energy-dispersive X-ray spectroscopy (EDX, Phenom Pro and XL). Thermogravimetric analysis (TGA, TA Instrument TGA Q500) was performed under nitrogen flow (60 mL/min) at a heating rate of 10 °C per min from room temperature to 800 °C in a platinum pan. Attenuated total reflectance-Fourier transformed infrared (ATR-FTIR, Thermo Nicolet 6700) spectroscopy was recorded in the range of 400–4000 cm^{-1}. The crystal

structure of pure TiO_2 nanoparticles was analyzed via X-ray diffraction (XRD, Shimadzu XRD-7000). The mean crystallite size was estimated from the broadening of the (101) and (200) peaks using Scherrer's equation.

Photocatalytic experiments

The photocatalytic activity of TiO_2/PANI-KpF nanocomposite for the degradation of MO (95%, Loba Chemie) and reduction in Cr(VI) ($K_2Cr_2O_7$, 99.5%, Loba Chemie) was investigated under dark and visible light. Blank and TiO_2-loaded (1.0 mg/mL) MO and Cr(VI) solutions were used as control. Experiments were carried out inside a laboratory-made visible light photocatalytic reactor equipped with a 6000 K LED lamp. In a typical experiment, TiO_2/PANI-KpF nanocomposite was immersed in 50 mL 10 ppm MO and Cr(VI) solutions at a catalyst loading of 1.0 mg/mL. At predetermined time intervals within 6 h (e.g., 0.5, 1, 2, 3, 4, and 6 h), a 1.0 mL aliquot was taken from each of the MO and Cr(VI) solutions. The temperature of the MO and Cr(VI) solutions was maintained at ambient conditions by placing them inside an ice bath during the photocatalytic experiment. The effect of varying TTIP concentrations on the photocatalytic activity of TiO_2/PANI-KpF nanocomposites was tested on MO solution under visible light illumination. Then, the nanocomposite with the highest photocatalytic activity was chosen for the photoreduction of Cr(VI) under visible light. Adsorption and photocatalytic experiments were performed twice. The concentration of the residual MO solution was calculated from the calibration curve of MO concentration with respect to its absorbance at 460 nm. On the other hand, the analysis of residual Cr(VI) concentration was performed using 1,5-diphenyl carbazide as the complexing agent. The complexation produced a violet-colored solution with an absorbance peak at 540 nm. The absorbance spectra of MO and Cr(VI) solutions were measured via UV–vis spectroscopy (Ocean Optics). The removal efficiency (RE, %) was calculated using the following equation:

$$RE = (C_o - C_t)/C_o \times 100\% \tag{1}$$

where C_o and C_t are the initial solution concentration (mg/L or ppm) and the solution concentration (mg/L or ppm) at time t (min), respectively.

The experimental data gathered under dark condition were fitted to the linearized pseudo-second-order kinetic model of adsorption, which is given by the following equation:

$$t/q_t = 1/k_2 q_e^2 + t/q_e \tag{2}$$

where q_t (mg/g) and q_e (mg/g) are the adsorption capacities at time t (min) and at chemical equilibrium, respectively, and k_2 (g/(mg·min)) represents the pseudo-second-order rate of adsorption [59].

On the other hand, the experimental data from the visible light-illuminated photocatalytic experiments were fitted into the Langmuir–Hinshelwood (L–H) kinetic model given by:

$$\ln\left(\frac{C_o}{C_t}\right) = k_1 t \qquad (3)$$

where C_o is the initial concentration of MO (ppm), C_t is the concentration of MO (ppm) at time t (min), and k_1 (min^{-1}) is the pseudo-first-order rate constant [60].

Antibacterial test

The antibacterial activity of TiO$_2$/PANI-KpF was tested on *Escherichia coli (E. coli)* UPCC 1195. A bacterial suspension approximating McFarland 2 (6.0×10^8 CFU/mL) was prepared from an 18–24 h old *E. coli*. Then, it was diluted to obtain a 10^6–10^7 CFU/mL cell suspension. Then, 0.4 g TiO$_2$/PANI-KpF was contacted with 20 mL *E. coli* suspension in a sterile Petri dish. The suspension was exposed to visible light for 6 h. A similar suspension containing the same amount of TiO$_2$/PANI-KpF was placed under dark conditions. After 6 h, the suspensions were serially diluted up to 10^5 and plated on nutrient agar (NA) before incubating at 35 °C for 24 h. Afterward, the *E. coli* colony-forming units (CFU) were counted using a Quebec counter.

Results and discussion

Immobilization of TiO$_2$ nanoparticles on PANI-KpF nanocomposite

Figure 1 shows the SEM image of the NaClO$_2$-treated KpF (NaClO$_2$-KpF), PANI-coated-KpF (PANI-KpF), and the TiO$_2$/PANI-KpF prepared with an increasing amount of TTIP. As shown in Fig. 1a, the surface of the NaClO$_2$-KpF microtube is relatively smooth, which indicates the presence of a waxy layer [54, 58]. Before
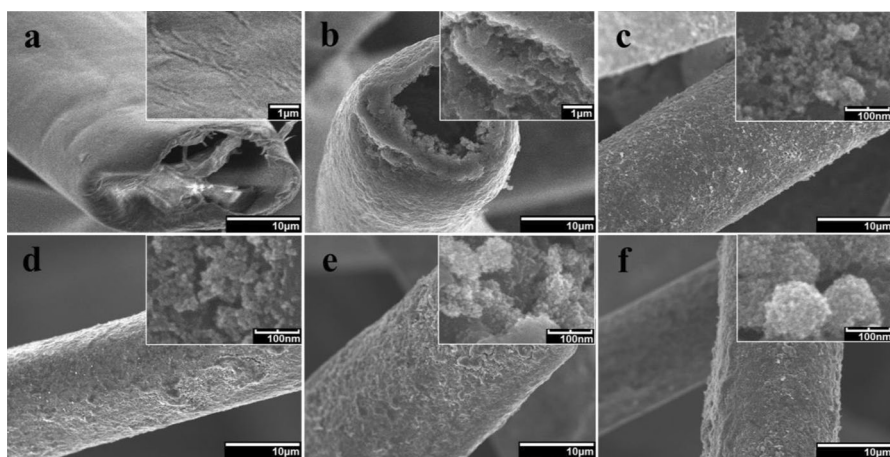

Fig. 1 SEM images of **a** NaClO$_2$-KpF, **b** PANI-KpF, and TiO$_2$/PANI-KpF nanocomposites prepared with **c** 0.5, **d** 1.0, **e** 1.5 and **f** 2.0 mL TTIP

the deposition of PANI, NaClO$_2$-treatment was employed to promote the adhesion of aniline monomer by removing the lignin content and expanding the amorphous region of the cellulose content of the fiber [32, 58, 61]. After the in situ oxidative polymerization of aniline on the surface of NaClO$_2$-KpF, a layer of compact and clustered PANI particles, with sizes in the range of tens to hundreds of nanometer, encapsulated the fiber while preserving its hollow microtubular structure (Fig. 1b).

After TiO$_2$ immobilization, it was observed that the PANI layer was retained regardless of the TTIP concentration. However, some PANI particles were detached from the surface of the kapok fiber after the hydrothermal reaction. This results in the reduction in the final mass of the nanocomposites from 400 to 353–361 mg. With increasing TTIP concentration, more TiO$_2$ agglomerates were deposited on the surface of the PANI-KpF nanocomposite. Higher magnification images show that these agglomerates are composed of nanoparticles with diameters of less than 50 nm.

Figure 2 shows the corresponding FTIR spectra of NaClO$_2$-KpF, PANI-KpF, and TiO$_2$/PANI-KpF nanocomposites prepared with different TTIP concentrations. The broad absorption bands of KpF at ~3330 and ~1035 cm^{-1} are attributed to the hydroxyl group (–OH) and C–O stretching vibrations in the cellulose region, respectively [58, 62–64]. The peaks at ~1730 and ~1370 cm^{-1} are associated with the carbonyl (C=O) group in the aliphatic aldehydes, esters, and ketones of plant wax, while the peak at ~1240 cm^{-1} is ascribed to the C–O stretching vibration in the
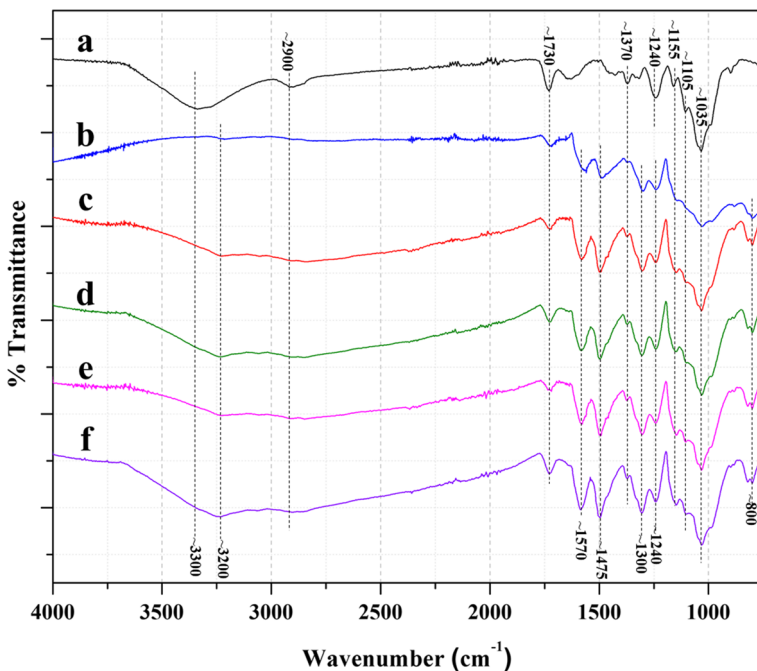

Fig. 2 FTIR spectra of **a** NaClO$_2$-KpF, **b** PANI-KpF, and TiO$_2$/PANI-KpF nanocomposites prepared with **c** 0.5, **d** 1.0, **e** 1.5 and **f** 2.0 mL TTIP

acetyl groups, which are also present in plant wax [54, 65]. In addition, the absorption band at ~2900 cm^{-1} is associated with the C–H stretching vibration of aliphatic CH_2 and CH_3 compounds in plant wax [54, 63, 65].

The successful deposition of PANI is confirmed by the presence of the absorption bands at ~1570 and ~1475 cm^{-1}, which are attributed to the C=N and C=C stretching of quinoid-ring and benzene-ring, respectively [32, 66–68]. Moreover, other important PANI absorption bands at ~1300, ~1240, and ~800 cm^{-1}, which are due to the C–N stretching of secondary aromatic amines, C–N^+ stretching in the polaron structure, and out-of-plane C–H vibration of symmetrically substituted benzene of PANI, respectively, are also present [66, 68, 69]. After the polymerization of aniline, the absorption peak of $NaClO_2$-KpF at ~3330, ~2900, and ~1370 cm^{-1} almost disappeared, while the absorption peak at ~1730 cm^{-1} decreased significantly. The IR peak of KpF at ~1240 cm^{-1} also overlapped with that of the PANI. These results suggest the adhesion of the PANI layer on the surface of KpF [66].

After the immobilization of TiO_2 nanoparticles, the PANI layer was relatively intact as indicated by the presence of its characteristic peaks in Fig. 2c–f, supporting the findings from the FE-SEM images (Fig. 1c–f). Then again, the increase in the intensity of the absorption bands at ~3330 and ~2900 cm^{-1} possibly indicates the reduction in the amount of PANI after the hydrothermal reaction. This agrees well with the decrease in the final mass of the nanocomposites. The intensity of the absorption band at ~1240 cm^{-1} was also decreased after the reaction. This implies the conversion of a large amount of emeraldine salt PANI into its emeraldine base form. This could be due to the de-doping of the polaron segment of PANI with OH^- ions, which were generated during the condensation of $Ti(OH)_4$ [70, 71].

Figure 3 shows the EDX spectra of the TiO_2/PANI-KpF nanocomposites with an increasing amount of TTIP. Peaks due to C, N, O, Ti, Cl, and S were identified from the spectra. The peaks of C and N atoms were mainly from the PANI chain. On the other hand, Ti and O peaks confirmed the presence of TiO_2 molecules. On the other hand, Cl and S peaks could be attributed to the Cl^- and SO_4^{2-} (or HSO_4^-) counter ions, which were released from the dissolution of HCl
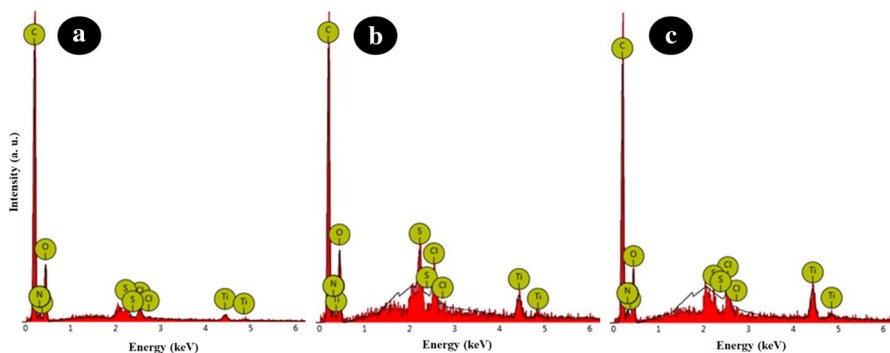

Fig. 3 EDX patterns of the TiO_2/PANI-KpF nanocomposites prepared with **a** 0.5, **b** 1.0 and **c** 2.0 mL TTIP. Insets show the corresponding SEM images (all at ×100 k magnification) of the nanocomposites at which the elemental analyses were conducted

Table 1 Average atomic concentrations of the elements present in the TiO$_2$/PANI-KpF nanocomposites prepared with 0.5, 1.0, and 2.0 mL TTIP

TTIP amount (mL)	Average atomic concentration (at.%)					
	C	N	O	Ti	Cl	S
0.5	64 ± 1	12 ± 0	21 ± 4	0.9 ± 0.6	1.0 ± 0.8	2.0 ± 1.3
1.0	62 ± 2	12 ± 2	24 ± 4	1.0 ± 0.4	0.9 ± 0.4	0.9 ± 0.5
2.0	60 ± 1	14 ± 1	24 ± 1	2.3 ± 0.5	1.3 ± 1.2	0.0 ± 0.0

Each average concentration was calculated from three EDX data taken from different areas on each nanocomposite
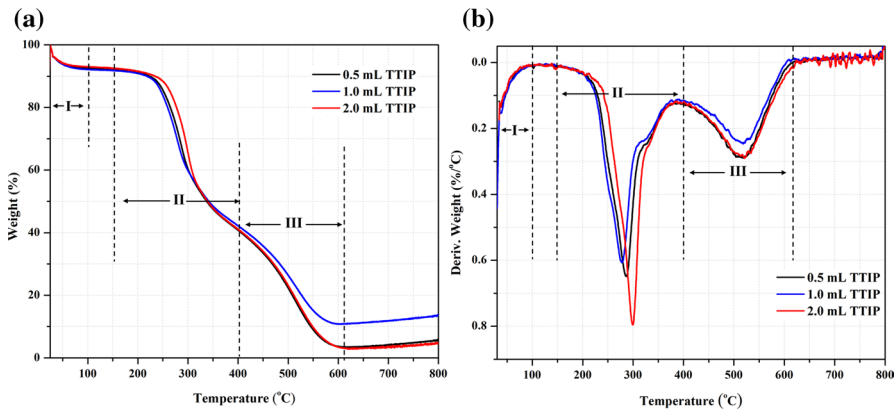

Fig. 4 **a** TGA thermograms and **b** DTG curves of the TiO$_2$/PANI-KpF nanocomposites prepared with different TTIP concentrations under N$_2$ flow

and APS during the polymerization of PANI [70]. Table 1 shows the average relative atomic concentration of the elements detected by EDX. With 0.5 and 1.0 mL TTIP, the average relative atomic concentration of Ti on the surface of PANI-KpF is about 1%. When 2.0 mL TTIP was added, the relative atomic concentration of Ti was increased to about 2%. This indicates that more TiO$_2$ nanoparticles were deposited on the surface of PANI-KpF at higher TTIP concentrations. These results correspond well with the observed FE-SEM images.

Figure 4 shows the TGA thermograms and corresponding DTG curves of the TiO$_2$/PANI-KpF prepared with varying amounts of TTIP. The thermograms of all the TiO$_2$/PANI-KpF nanocomposites exhibit three degradation stages. The weight loss in stage I (30 to 100 °C) is attributed to the evaporation of adsorbed water onto the samples [60]. Further, the weight loss in stage II (150 to 400 °C) was due to the thermal degradation of cellulose and hemicellulose contents of kapok fiber [72, 73]. The main peak, which exhibits a minimum at around 300 °C, is associated with the degradation of hemicellulose [72]. On the other hand, the shoulder with a minimum located at around 330 °C is associated with the degradation of cellulose. Finally, the weight loss in stage III (400 to 620 °C) is attributed to the thermal degradation of the backbone chains of PANI [74, 75]. The

remaining weight of the samples from around 620 °C onwards may correspond to the presence of inorganic contents (i.e., TiO_2 nanoparticles) and carbon-containing residues. The significant increase in the amount of remaining materials when the TTIP concentration was increased from 0.5 to 1.0 mL possibly suggests a higher concentration of immobilized TiO_2 nanoparticles on the surface of PANI-KpF. However, upon increasing the TTIP concentration to 2.0 mL, the amount of residues decreased. This is possibly due to the decrease in the amount of immobilized TiO_2 nanoparticles. As seen from the FE-SEM images, the TiO_2 nanoparticles agglomerated at higher TTIP concentrations. These agglomerated TiO_2 nanoparticles could have detached from the surface of PANI-KpF due to the weak adhesion. As a result, fewer TiO_2 nanoparticles were actually on the surface of PANI-KpF.

The TEM image and XRD pattern of pure TiO_2 nanoparticles synthesized by the same hydrothermal process in the absence of PANI-KpF are shown in Fig. 5. It can be observed in Fig. 5a that the TiO_2 nanoparticles are spherical with diameters ranging from 5 to 10 nm. Moreover, the inset shows the well-defined crystalline orientation of a single crystal TiO_2 nanoparticle with a measured d-spacing of 0.355 nm. This corresponds to the (101) plane of anatase TiO_2. As shown in Fig. 5b, relatively broad diffraction peaks were obtained, which indicates a very small crystallite size as confirmed by the TEM image.

In Fig. 5b, the two most intense single diffraction peaks at $2\theta = 25.31$ and $47.95°$ represent the (101) and (200) peaks of anatase TiO_2 (JCPDS card no. 78–2486), respectively. Based on the broadening of these peaks, the mean crystallite size of the nanoparticles was estimated to be about 6.06 nm using Scherrer's formula. This value is well within the range of diameters measured from the TEM images. This indicates that some of the TiO_2 nanoparticles are single crystals. Other XRD peaks at $2\theta = 37.97, 54.09, 55.06, 62.80, 68.97, 70.04, 75.31,$ and $82.77°$ were identified to be reflections of the (004), (105), (211), (204), (116), (220), (215), and (224) peaks of pure anatase TiO_2, respectively. Then again, most of these peaks are the
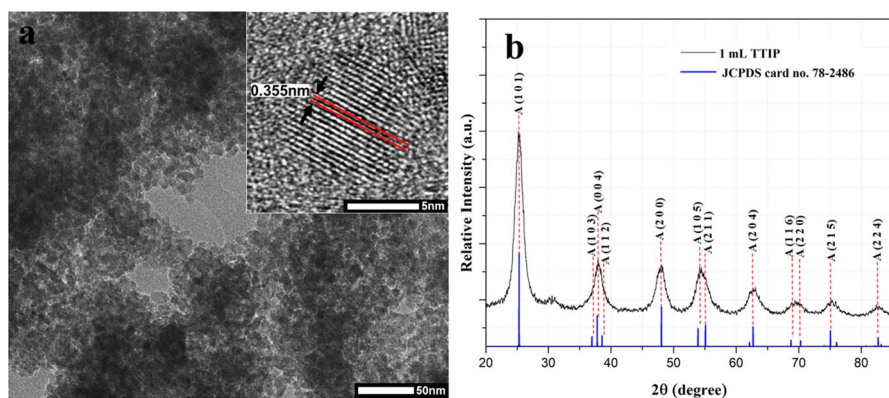

Fig. 5 **a** TEM image (inset: d-spacing of the (101) plane) and **b** X-ray diffraction pattern of TiO_2 nanoparticles prepared with 1.0 mL TTIP
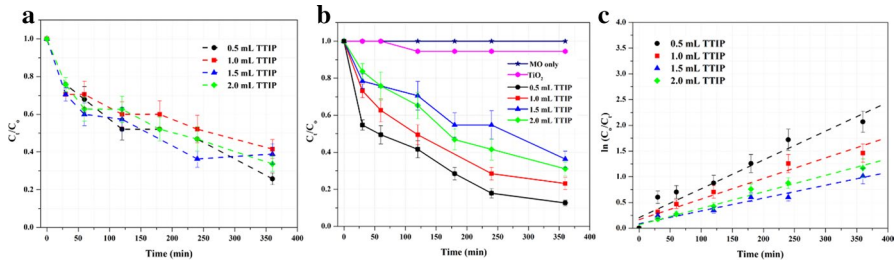
Fig. 6 Removal of MO by TiO$_2$/PANI-KpF prepared with different concentrations of TTIP under **a** dark conditions and **b** visible light illumination in the presence of iced water bath. **c** Langmuir–Hinshelwood kinetic model of MO removal by TiO$_2$/PANI-KpF prepared with different TTIP concentrations under visible light-illuminated conditions

Table 2 Calculated pseudo-second-order adsorption kinetic (dark condition) and L–H pseudo-first-order kinetic (visible light-illuminated condition) model parameters for the removal of MO by TiO$_2$/PANI-KpF prepared with different concentrations of TTIP

TTIP amount (mL)	Pseudo-second-order adsorption kinetics (dark)				L–H pseudo-first-order kinetics (Visible)		
	RE (%)	q_e (mg/g)	k_2 (g/mg min)	R^2	RE (%)	k_1 (min^{-1})	R^2
0.5	74.2	6.41	0.0030	0.9905	87.4	0.0056	0.9555
1.0	58.4	5.50	0.0046	0.9854	76.8	0.0040	0.9540
1.5	61.0	6.02	0.0049	0.9761	63.7	0.0025	0.9548
2.0	66.3	6.20	0.0036	0.9960	68.9	0.0032	0.9787

summation of several (2 to 3) diffraction peaks. which led to the overall broadening. No diffraction peaks corresponding to other TiO$_2$ phases, such as rutile and brookite, were observed.

Kinetic studies of MO removal by TiO$_2$/PANI-KpF nanocomposite

Figure 6 shows the removal of MO under dark and visible light. Under dark conditions, the removal of MO was mainly due to adsorption. This was confirmed by the high R^2 values when the kinetic data under the dark condition were fitted into the linearized pseudo-second-order kinetic model of adsorption. It was demonstrated in the previous study that the adsorption of MO dye onto the PANI-KpF nanocomposite follows the pseudo-second-order kinetic model, which suggests the diffusion of MO molecules within the porous structure of the PANI coating [32, 76]. In our previous work, the PANI-KpF nanocomposite attained an adsorption capacity for MO of about 137 mg/g [32].

After 6 h of adsorption, the removal efficiency (RE) was in the range of 58.4–74.2% for the TiO$_2$/PANI-KpF nanocomposites as shown in Table 2. Furthermore, the sample prepared with 0.5 mL TTIP showed the best performance with a removal efficiency of 74.2%. As discussed in the previous section, some PANI

particles were detached from the kapok surface during the deposition of TiO_2 nanoparticles, particularly at higher TTIP concentrations. Thus, the high removal efficiency of the sample with 0.5 mL TTIP could be attributed to the relatively larger amount of PANI retained on the surface of the nanocomposite.

Under visible light illumination, there was no observable change in the concentration of blank MO solution after 6 h as seen in Fig. 6b. This indicates that there was no induced self-degradation of MO under visible light. With 50 mg pure anatase TiO_2 nanoparticles, only about 5.2% removal efficiency was achieved. Due to the wide bandgap (3.2 eV) of anatase TiO_2, the energy of visible light was not sufficient to excite the electrons from its valence band to its conduction band. Therefore, the reduction in the concentration of MO might be due to the adsorption of MO molecules onto the TiO_2 nanoparticles. This explains the low removal efficiency. By applying the pseudo-second order adsorption kinetic model on the removal of MO by pure TiO_2, an adsorption capacity and R^2 value of 0.56 mg/g and 0.9981 were calculated, respectively.

The influence of TTIP concentration in the photocatalytic activity of TiO_2/PANI-KpF is apparent in Fig. 6b. For the samples prepared with 0.5 and 1.0 mL TTIP, about 13.0 and 18.0% increase in removal efficiency for MO were achieved under visible light compared to dark conditions. This substantial improvement in removal efficiencies could be attributed to the photocatalytic degradation of MO over the TiO_2/PANI photocatalyst. This indicates that PANI could effectively photosensitize the TiO_2 nanoparticles immobilized on the PANI surface by producing electron–hole pairs under visible light illumination.

With a bandgap in the range of 1.3 (doped or protonated) to 2.7 eV (undoped), PANI exhibits strong absorption for visible light [27]. When TiO_2 is coupled with PANI, the photoexcited electrons in the conduction band of PANI can easily jump to the conduction band of TiO_2 due to the more negative band edge of PANI [60]. On the other hand, the electrons in the valence band of TiO_2 can migrate to the valence band of PANI and combine with the photoexcited PANI holes [77, 78]. Subsequently, holes are generated in the TiO_2 valence band. The photoexcited holes in both PANI and TiO_2 valence bands can independently react with surface-bound water molecules or OH^- ions to form hydroxyl radicals (·OH), while the photoexcited electrons in the conduction bands of PANI and TiO_2 can react with oxygen molecules to produce superoxides (O_2^-) [77]. Due to its high oxidizing ability, ·OH can attack the electron-rich aromatic rings and azo bonds ($N = N$) of MO molecule by substitution reaction [60, 79]. The generated intermediates would then undergo ring-opening due to their instability, leading to the complete mineralization of MO. In addition to CO_2 and H_2O, the mineralization of MO would lead to the formation of SO_4^{2-}, NO_3^-, and NH_4^+ species [80, 81]. Additionally, the excellent adsorption capability of PANI could increase the amount of MO molecules near the photoactive layer of the TiO_2 nanoparticles. Consequently, the rate of MO decoloration was increased. Aside from the enhanced photocatalytic activity of immobilized TiO_2, the utilization of PANI-KpF as a carrier also improved handling during recovery compared with pure TiO_2 nanopowder.

However, with 1.5 and 2.0 mL TTIP, a < 3.0% increase in the removal efficiencies was achieved. This could be due to the agglomeration of TiO_2 nanoparticles on the

PANI surface as previously seen from the FE-SEM images in Fig. 1. The formation of agglomerates possibly decreased the contact between PANI and TiO_2. In addition, the opacity of the TiO_2 layer probably increased, which hindered the penetration of visible light into the PANI matrix [60]. This would lead to the decline in the generation of photoexcited electron–hole pairs within the polymer and the overall photocatalytic activity of the nanocomposite.

The kinetics of MO removal by combined adsorption and photodegradation was further analyzed by fitting the data from Fig. 6b into the Langmuir–Hinshelwood (L–H) kinetic model.

The $\ln(C_o/C_t)$ versus time plots of MO removal by TiO_2/PANI-KpF prepared with different TTIP concentrations under visible light are shown in Fig. 6c. Relatively high linearity was achieved for all the L–H kinetic model plots as indicated by their corresponding R^2 values (>0.95) shown in Table 2. This confirms the photodegradation of MO by TiO_2/PANI, which follows the pseudo-first-order kinetic reaction. The TiO_2/PANI-KpF nanocomposite prepared with 0.5 mL TTIP achieved the highest pseudo-first-order rate constant of about 0.0056 min^{-1}.

Kinetic studies of Cr(VI) removal by TiO_2/PANI-KpF nanocomposite

The TiO_2/PANI-KpF nanocomposite prepared with 1.0 mL TTIP was chosen for the removal of Cr(VI). Similarly, the initial concentration and volume of the Cr(VI) solution (pH ~ 6) was set to 10 ppm and 50 mL, respectively. The experiments were conducted for 6 h under dark and visible light using an iced bath to maintain the temperature at ambient conditions. Blank and TiO_2-loaded Cr(VI) solutions were also used as controls. As seen in Fig. 7a, there was no apparent change in the initial concentration of Cr(VI) after 6 h. This suggests the absence of any degradation or reduction in Cr(VI) ions. Further, using pure TiO_2 powder at 1.0 mg/mL catalyst loading, only 1.2% removal efficiency was achieved. This could also be attributed to the adsorption of Cr(VI) onto the TiO_2 nanoparticles. By applying
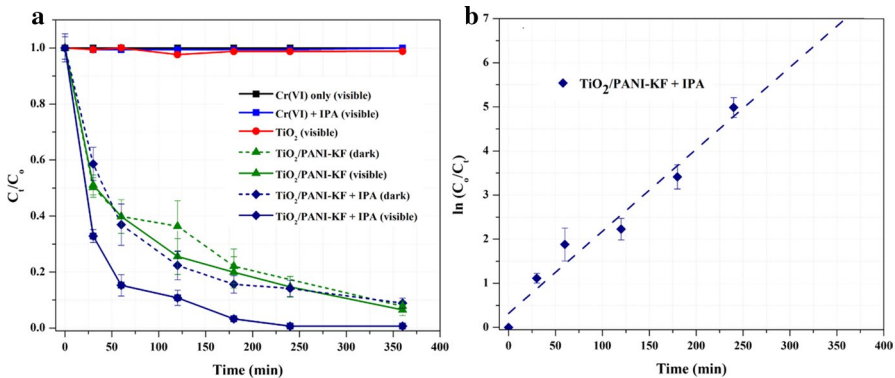

Fig. 7 a Removal of Cr(IV) by pure TiO_2 powder and TiO_2/PANI-KpF (with and without IPA) as a function of time under dark and visible light; and **b** the corresponding L–H kinetic model plot for TiO_2/PANI-KpF (with IPA) under visible
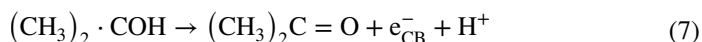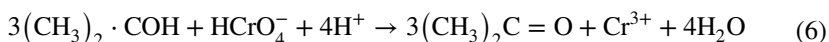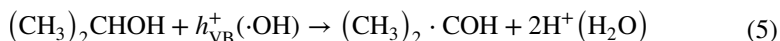
the pseudo-second-order kinetic model, an adsorption capacity and R^2 value of 0.14 mg/g and 0.9957 were determined, respectively.

Using TiO_2/PANI-KpF nanocomposite, there was no significant difference in the amount of Cr(VI) removed under dark and visible light. Removal efficiencies of around 92.2 and 93.5% were achieved under dark and visible light, respectively. This suggests that the removal of Cr(VI) was mainly due to adsorption and the photo-reduction of Cr(VI) was negligible or possibly did not proceed at all. At pH 6, Cr(VI) exists as hydrogen chromate ($HCrO_4^-$) and chromate (CrO_4^{2-}) anions [66]. Both species could be effectively adsorbed onto PANI through electrostatic attraction. The adsorption data were also fitted into the pseudo-second-order kinetic model. Adsorption capacities of 10.20 and 10.21 mg/g with R^2 values of 0.9848 and 0.9966 for dark and visible light conditions were achieved, respectively.

Generally, to photo-reduce heavy metal ions, the energy level of the photoexcited electrons should be more negative than the reduction potentials of the metal ions [82]. As pH is increased from 0 to 6, the position of the conduction band energy level of TiO_2 decreases from −0.050 to −0.404 V [83]. On the other hand, the reduction potential of Cr(VI) decreases from 1.35 to 0.52 V as the pH is changed from 0 to 6 [83]. Although the photo-reduction of Cr(VI) to Cr(III) as in Eq. (4) is thermodynamically feasible at a potential difference of − 0.922 V, the reaction possibly proceeds at a very slow rate [83, 84].

$$HCrO_4^- + 7H^+ + 3e_{CB}^- \rightarrow Cr^{3+} + 4H_2O \qquad (4)$$
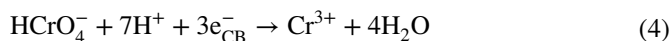
The photocatalytic reduction in Cr(VI) to Cr(III) could be enhanced with the introduction of organic hole scavengers, such as 2-propanol [IPA, $(CH_3)_2CHOH$] [85]. In the presence of 1.0 mL IPA (0.26 mmol/L) under visible light, a removal efficiency of more than 99% was reached within 4 h of illumination. After 6 h, Cr(VI) was completely removed. In addition to the significant reduction in electron–hole recombination following the addition of IPA, the reaction of a hole scavenger with holes or ·OH radical produces derivatives that possess highly negative reducing potentials [85, 86]. As described by Eq. (5), the oxidation of IPA [$(CH_3)_2CHOH$] by holes or ·OH radicals produces 1-hydroxyalkyl radical [$(CH_3)_2$·COH] with a corresponding reducing potential [$E^o(CH_3)_2C=O/(CH_3)_2$·COH] of −1.6 V [81]. Subsequently, this free radical can directly reduce Cr(VI) to Cr(III) Eq. (6) or further increase the number of electrons in the conduction band Eq. (7) [85].

$$\left(CH_3\right)_2CHOH + h_{VB}^+(\cdot OH) \rightarrow \left(CH_3\right)_2 \cdot COH + 2H^+\left(H_2O\right) \qquad (5)$$

$$3\left(CH_3\right)_2 \cdot COH + HCrO_4^- + 4H^+ \rightarrow 3\left(CH_3\right)_2C=O + Cr^{3+} + 4H_2O \qquad (6)$$

$$\left(CH_3\right)_2 \cdot COH \rightarrow \left(CH_3\right)_2C=O + e_{CB}^- + H^+ \qquad (7)$$

A Cr(VI) solution in the presence of IPA only was also prepared under visible light to determine whether the hole scavenger could induce the reduction in Cr(VI) in the absence of TiO_2/PANI-KpF. The concentration of Cr(VI) solution

remained the same after 6 h of illumination as seen in Fig. 7a. This indicates that IPA did not undergo self-oxidation to produce reducing radicals. Likewise, IPA had no apparent effect on the removal of Cr(VI) in the presence of TiO_2/PANI-KpF under dark conditions. This implies that the reaction between TiO_2/PANI and IPA to produce reducing radicals did not take place without the generation of photoexcited electron–hole pair. Thus, in the absence of light and/or photocatalyst, IPA did not act as a hole or ·OH radical scavenger.

The removal of Cr(VI) by TiO_2/PANI-KpF under visible light was also analyzed using the L–H kinetic model. The corresponding $\ln(C_o/Ct)$ vs time plot for the removal of Cr(VI) is shown in Fig. 7b. With an R^2 value of 0.9630, the result suggests that the photo-reduction of Cr(VI) by TiO_2/PANI-KpF under visible light in the presence of IPA follows the Langmuir–Hinshelwood kinetic model. The calculated L–H kinetic model parameters for the removal of Cr(VI) under visible light illumination are shown in Table 3.

Antibacterial activity

The enhancement of the antibacterial activity of TiO_2/PANI-KpF under visible light was investigated by counting the colonies formed by *E. coli* bacteria after contacting 10^6–10^7 CFU/mL bacterial suspension with the nanocomposite for 6 h. Figure 8 shows the marked colony-forming units (CFU) of *E. coli* bacteria after 6 h of exposure to dark and visible light in the presence of TiO_2/PANI-KpF. Under dark conditions, around 65 ± 5 CFU, which is equivalent to an actual *E. coli* concentration of $\sim 6.6 \times 10^6$ CFU/mL, was observed. This indicates a minimal decrease in the number of bacteria after exposure to TiO_2/PANI-KpF in the dark. On the other hand, only 46 ± 9 CFU or $\sim 4.6 \times 10^6$ CFU/mL of *E. coli* remained after visible light illumination. The ~30% reduction in *E. coli* concentration suggests the antibacterial activity of TiO_2/PANI-KpF against *E. coli* bacteria under visible light, which is primarily linked to the oxidative damage on bacterial cells by the generated ·OH radicals [87–90].

Table 3 Calculated pseudo-second-order adsorption and L–H pseudo-first-order kinetic model parameters for the removal of Cr(VI) by TiO_2/PANI-KpF

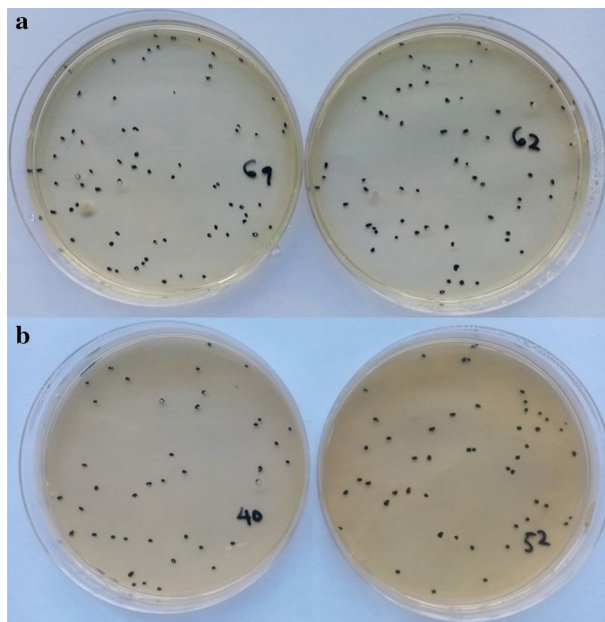| Condition	k_2 (g/mg min)	R^2
Dark	0.0021	0.9848
Dark (with IPA)	0.0026	0.9992
Visible light	0.0024	0.9966
	k_1 (min^{-1})	R^2
Visible light (with IPA)	0.0186	0.9630

Fig. 8 Counted *E. coli* CFU on nutrient agar after 6 h of contacting with TiO_2/PANI-KpF under **a** dark and **b** visible light illumination for 6 h

Conclusion

TiO_2 nanoparticles were successfully immobilized on the surface of PANI-KpF via a hydrothermal reaction method. The TiO_2 nanoparticles appeared as large agglomerates on the surface on PANI-KpF, particularly at higher TTIP concentration. Under dark conditions, the removal of MO and Cr(VI) was mainly due to adsorption, which follows the pseudo-second-order kinetic reaction. After 6 h of adsorption, the removal efficiency was in the range of 58.4–74.2% for MO, whereas 92.2% for Cr(VI). Enhanced MO removal up to 87.4% was achieved due to photodegradation under visible light for 6 h. On the other hand, the photocatalytic reduction in Cr(VI) by TiO_2/PANI-KpF was insignificant under visible light. With the addition of IPA as ·OH radical or hole scavenger, reduction in Cr(VI) was achieved under visible light with 100% removal. Lastly, the TiO_2/PANI-KpF nanocomposite demonstrated a possible antibacterial activity against *E. coli* bacteria with around 30% CFU reduction under visible light compared to dark conditions.

References

1. Ajmal A, Majeed I, Malik RN, Idriss H, Nadeem MA (2014) Principles and mechanisms of photocatalytic dye degradation on TiO_2 based photocatalysts: a comparative overview. RSC Adv 4(70):37003–37026
2. Barakat MA (2011) New trends in removing heavy metals from industrial wastewater. Arab J Chem 4:361–377
3. Pelaez M, Nolan NT, Pillai SC, Seery MK, Falaras P, Kontos AG, Dunlop PSM, Hamilton JWJ, Byrne JA, O'Shea K, Entezari MH, Dionysiou DD (2012) A review on the visible light active titanium dioxide photocatalysts for environmental applications". Appl Catal B Environ 125:331–349
4. Hayamun M, Raziq F, Khan A, Luo W (2018) Modification strategies of TiO_2 for potential applications in photocatalysis: a critical review. Green Chem Lett Rev 11(2):86–102
5. Bai Y, Mora-Sero I, Angelis FD, Bisquert J, Wang P (2014) Titanium dioxide nanomaterials for photovoltaic applications. Am Chem Soc Chem Rev 114:10095–10130
6. Li X, Wang D, Cheng G, Luo Q, An J, Wang Y (2008) Preparation of polyaniline-modified TiO_2 nanoparticles and their photocatalytic activity under visible light illumination. Appl Catal B Environ 81:267–273
7. Bhatia V, Dhir A (2016) Transition metal doped TiO_2 mediated photocatalytic degradation of anti-inflammatory drug under solar irradiations. J Environ Chem Eng 4:1267–1273
8. Tseng LT, Luo X, Bao N, Ding J, Li S, Yi J (2016) "Structures and properties of transition-metal-doped TiO_2 nanorods. Mater Lett 170:142–146
9. Li X, Zhuang Z, Li W, Pan H (2012) Photocatalytic reduction of CO_2 over noble metal-loaded and nitrogen-loaded mesoporous TiO_2. Appl Catal A Gen 429:31–38
10. Gomes JF, Lopes A, Bednarczyk K, Gmurek M, Stelmachowski M, ZaleskaMedynska A, Quinta-Ferreira ME, Costa R, Quinta-Ferreira RM, Martins RC (2018) Effects of noble metals (Ag, Pd, Pt) loading over the efficiency of TiO2 during photocatalytic ozonation on the toxicity of parabens. Chemengineering 2(10):4
11. Szkoda M, Siuzdak K, Lisowska-Oleksiak A (2016) Non-metal doped TiO_2 nanotube arrays for high efficiency photocatalytic decomposition of organic species in water. Phys E 84:141–145
12. El-Sheikh SM, Zhang G, El-Hosainy HM, Ismail AA, O'Shea KE, Falaras P, Kontos AG, Dionysiou DD (2014) High performance sulfur, nitrogen and carbon doped mesoporous anatase-brookite TiO_2 photocatalyst for the removal of microcystin-LR under visible light irradiation. J Hazard Mater 280:723–733
13. Kubacka A, Caudillo-Flores U, Barba-Nieto I, Fernández-García M (2021) Towards full-spectrum photocatalysis: Successful approaches and materials. Appl Catal A Gen. https://doi.org/10.1016/j.apcata.2020.117966
14. Wang Z, Lang X (2018) Visible light photocatalysis of dye-sensitized TiO_2: the selective aerobic oxidation of amines to imines. Appl Catal B Environ 224:404–409
15. Choi SK, Yang HS, Kim JH, Park H (2012) Organic dye-sensitized TiO_2 as a versatile photocatalyst for solar hydrogen and environmental remediation. Appl Catal B Environ 121:206–213
16. Neves MC, Nogueira JMF, Trindade T, Mendonca MH, Pereira MI, Monteiro OC (2009) Photosensitization of TiO_2 by Ag_2S and its catalytic activity on phenol photodegradation. J Photochem Photobiol A Chem 204:168–173
17. Chen H, Li W, Liu H, Zhu L (2011) Performance enhancement of CdS-sensitized TiO_2 mesoporous electrode with two different sizes of CdS nanoparticles. Microp Mesop Mater 138:235–238
18. Zainudin SNF, Markom M, Abdullah H, Adami R, Tasirin SM (2013) Optimized synthesis and photovoltaic performance of TiO_2 nanoparticles for dye-sensitized solar cell. Particuology 11:753–759
19. Sanjay P, Deepa K, Madhavan J, Senthil S (2018) Performance of TiO_2 based dye-sensitized solar cells fabricated with dye extracted from leaves of Peltophorum pterocarpum and Acalypha amentacea as sensitizer. Mater Lett 219:158–162
20. Peng B, Jungmann G, Jager C, Haarer D, Schmidt HW, Thelakkat M (2004) Systematic investigation of the role of compact TiO_2 layer in solid state dye-sensitized TiO_2 solar cells. Coord Chem Rev 248(13–14):1479–1489
21. Oku T, Kakuta N, Kobayashi K, Suzuki A, Kikuchi K (2011) Fabrication and characterization of TiO_2-based dye-sensitized solar cells. Prog Natl Sci Mater Int 21(2):122–126
22. Pei D, Luan J (2012) Development of visible light-responsive sensitized photocatalysts. Int J Photoenergy 2012:262831

23. Deng Y, Tang L, Zeng G, Dong H, Yan M, Wang J, Hu W, Wang J, Zhou Y, Tang J (2016) Enhanced visible light photocatalytic performance of polyaniline modified mesoporous single crystal TiO_2 microsphere. Appl Surf Sci 387:882–893

24. Deng F, Li Y, Luo X, Yang L, Tu X (2013) Preparation of conductive polypyrrole/TiO_2 nanocomposite via surface molecular imprinting technique and its photocatalytic activity under simulated solar light irradiation. Coll Surf A Physicochem Eng Asp 395:183–189

25. Boeva ZA, Sergeyev VG (2014) Polyaniline: synthesis, properties, and application. Polym Sci C 56(1):144–153

26. Bhadra S, Khastgir D, Singha NK, Lee JH (2009) Progress in preparation, processing and applications of polyaniline. Prog Polym Sci 34:783–810

27. Kwon O, McKee ML (2000) Calculations of band gaps in polyaniline from theoretical studies of oligomers. J Phys Chem B 104:1686–1694

28. Ahmad I, Kan CW (2017) Visible-light-driven, dye-sensitized TiO_2 photo-catalyst for self-cleaning cotton fabrics. Coatings 7:192

29. Morsi RE, Elsabee MZ (2015) Polyaniline nanotubes: mercury and competitive heavy metals uptake. Am J Polym Sci 5(1):10–17

30. Zheng YA, Liu Y, Wang AQ (2012) Kapok fiber oriented polyaniline for removal of sulfonated dyes. Ind Eng Chem Res 51(30):10079–10087

31. Herrera MU, Futalan CM, Gapusan R, Balela MDL (2018) Removal of methyl orange and copper (II) ions from aqueous solution using polyaniline-coated kapok (Ceiba pentandra) fibers. Wat Sci Tech 78:1137–1147

32. Gapusan RB, Balela MDL (2020) Adsorption of anionic methyl orange dye and lead(II) heavy metal ion by polyaniline-kapok fiber nanocomposite. Mater Chem Phys 243:122682

33. Lacuesta AC, Herrera MU, Manalo R, Balela MDL (2018) Fabrication of kapok paper-zinc oxide-polyaniline hydrid nanocomposite for methyl orange removal. Surf Coatings Tech 350:971–976

34. Li YF, Liu ZP (2011) Particle size, shape and activity for photocatalysis on titania anatase nanoparticles in aqueous surroundings. J Am Chem Soc 133:15743–15752

35. Cabello-Alvarado CJ, Quiñones-Jurado ZV, Cruz-Delgado VJ, Avila-Orta CA (2020) Pigmentation and degradative activity of TiO_2 on polyethylene films using Masterbatches fabricated using variable-frequency ultrasound-assisted melt-extrusion. Materials 13(17):3855

36. Chauhan I, Mohanty P (2014) Immobilization of titania nanoparticles on the surface of cellulose fibres by a facile single step hydrothermal method and study of their photocatalytic and antibacterial activities. R Soc Chem Adv 4:57885–57890

37. Andrade-Guel M, Díaz-Jiménez L, Cortés-Hernández D, Cabello-Alvarado C, Ávila-Orta C, Bartolo-Pérez P, Gamero-Melo P (2019) Microwave assisted sol-gel synthesis of titanium dioxide using hydrochloric and acetic acid as catalysts. Boletín de la Sociedad Española de Cerámica y Vidrio 58(4):171–177

38. Endrodi B, Kecsenovity E, Rajeshwar K, Janaky C (2018) One-step electrodeposition of nanocrystalline TiO_2 films with enhanced photoelectrochemical performance and charge storage". ACS Appl Energy Mater 1:851–858

39. He F, Ma F, Li T, Li G (2013) Solvothermal synthesis of N-doped TiO_2 nanoparticles using different nitrogen sources, and their photocatalytic activity for degradation of benzene. Chin J Catal 34:2263–2270

40. Lee H, Song MY, Jurng J, Park YK (2011) The synthesis and coating process of TiO_2 nanoparticles using CVD process. Powder Technol 214:64–68

41. Zhang H, Yan H, Mao N (2014) Functional modification with TiO_2 nanoparticles and simultaneously dyeing of wool fibers in a one-pot hydrothermal process. Ind Eng Chem Res 53:2030–2041

42. El-Roz M, Haidar Z, Lakiss L, Toufaily J, Thibault-Starzyk F (2013) Immobilization of TiO_2 nanoparticles on natural Luffa cylindrical fibers for photocatalytic applications. R Soc Chem Adv 3:3438–3445

43. Shahrezaei M, Habibzadeh S, Babaluo AA, Hosseinkhani H, Haghighi M, Hasanzadeh A, Tahmasebpour R (2017) "Study of synthesis parameters and photocatalytic activity of TiO_2 nanostructures. J Exp Nanosci 12(1):45–61

44. Supothina S, Rattanakam R, Tawkaew S (2012) Hydrothermal synthesis and photocatalytic activity of anatase TiO_2 nanofiber. J Nanosci Nanotechnol 12:4998–5003

45. Arguelles KE, Herrera MU, Futalan CCM, Balela MDL (2017) Fabrication of polyaniline-coated kapok (Ceiba pentandra) fibers embedded with copper-based particles. IOP Conf Ser Mater Sci Eng 201:012042

46. Agcaoili AR, Herrera MU, Futalan CM, Balela MDL (2017) Fabrication of polyacrylonitrile-coated kapok hollow microtubes for adsorption of methyl orange and Cu(II) ions in aqueous solution. J Taiwan Inst Chem Eng 78:359–359

47. Osman E, Moriga T, Murai K, Rashid MWA, Manaf MEA, Horikawa T (2018) "Photocatalytic activity of nanostructured tubular TiO_2 synthesized using kenaf fibers as a sacrificial template. Ind Crops Prod 113:210–216

48. Liu X, Cui Y, Hao S, Chen H (2018) Influence of depositing nano-SiO_2 particles on the surface microstructure and properties of jute fibers via in situ synthesis. Compos A 109:368–375

49. Luo S, Chen S, Chen Y, Chen S, Ma N, Wu Q (2016) "Sisal fiber-based solid amine adsorbent and its kinetic adsorption behaviors for CO_2. R Soc Chem Adv 6:72022–72029

50. Yang M, Liu W, Jiang C, He S, Xie Y, Wang Z (2018) Fabrication of superhydrophobic cotton fabric with fluorinated TiO_2 sol by a green and one-step sol-gel process. Carbohyd Polym 197:75–82

51. Zhang X, Duan C, Zhao N, Xiao H, Shi M (2010) Facile fabrication of large scale microtubes with a natural template-kapok fiber. Chin J Polym Sci 28(5):841–847

52. Yang Z, Yan J, Wang F (2018) Pore structure of kapok fiber. Cellulose 25(6):3219–3227

53. Meiwu S, Hong X, Weidong Y (2010) The fine structure of the kapok fiber. Text Res J 80(2):159–165

54. Lim TT, Huang X (2007) Evaluation of hydrophobicity/oleophilicity of kapok and its performance in oily water filtration: comparison of raw and solvent-treated fibers. Ind Crop Prod 26:125–134

55. Sunmonu OK, Abdullahi D (1992) Characterization of fibres from the plant Ceiba pentandra. J Tex Inst 83(2):273–274

56. Balela MDL, Intila NM, Salvanera SR (2019) Adsorptive removal of lead ions in aqueous solution by kapok-polyacrylonitrile nanocomposites. Mater Today Proc 17:672–678

57. Fan H, Yu X, Long Y, Zhang X, Xiang H, Duan C, Zhao N, Zhang X, Xu J (2012) Preparation of kapok-polyacrylonitrile core-shell composite microtube and its application as gold nanoparticles carrier. Appl Surf Sci 258:2876–2882

58. Liu Y, Wang J, Zheng Y, Wang A (2012) Adsorption of methylene blue by kapok fiber treated by sodium chlorite optimized with response surface methodology. Chem Eng J 184:248–255

59. Ho YS, McKay G (1999) Pseudo-second order model for sorption process". Process Biochem 34:451–465

60. Sboui M, Nsib MF, Rayes A, Swaminathan M, Houas A (2017) TiO_2-PANI/cork composite: a new floating photocatalyst for the treatment of organic pollutants under sunlight irradiation. J Environ Sci 60:3–13

61. Wang J, Zheng Y, Wang A (2012) Effect of kapok fiber treated with various solvents on oil absorbency. Ind Crops Prod 40:178–184

62. Bono A, Ying PH, Yan FY, Muei CL, Sarbatly R, Krishnaiah D (2009) Synthesis and characterization of carboxymethyl cellulose from palm kernel cake. Adv Natl Appl Sci 3(1):5–11

63. Mwaikambo LY, Ansell MP (2002) Chemical modification of hemp, sisal, jute, and kapok fibers by alkalization. J Appl Polym Sci 84:2222–2234

64. Rosa MF, Medeiros ES, Malmonge JA, Gregorski KS, Wood DF, Mattoso LHC, Glenn G, Orts WJ, Imam SH (2010) Cellulose nanowhiskers from coconut husk fibers: effect of preparation conditions on their thermal and morphological behavior. Carbohydr Polym 81:83–92

65. Abdullah MA, Rahmah AU, Man Z (2010) Physicochemical and sorption characteristics of Malaysian *Ceiba pentandra* (L.) Gaertn. as a natural oil sorbent. J Hazard Mater 177:683–691

66. Zheng Y, Wang W, Huang D, Wang A (2012) Kapok fiber oriented-polyaniline nanofibers for efficient Cr(VI) removal. Chem Eng J 191:154–161

67. Yoon SB, Yoon EH, Kim KB (2011) Electrochemical properties of leucoemeraldine, emeraldine, and pernigraniline forms of polyaniline/multi-wall carbon nanotube nanocomposites for supercapacitor applications. J Power Sour 196:10791–10797

68. Blinova NV, Stejskal J, Trchová M, Prokeš J, Omastová M (2007) Polyaniline and polypyrrole: a comparative study of the preparation. Eur Polym J 43:2331–2341

69. Quillard S, Louarn G, Lefrant S (1994) Vibrational analysis of polyaniline: a comparative study of leucoemeraldine, emeraldine and pernigraniline bases. Phys Rev B 50(17):12496–12508

70. Tang SJ, Wang AT, Lin SY, Huang KY, Yang CC, Yeh JM, Chiu KC (2011) Polymerization of aniline under various concentrations of APS and HCl". Polym J 43:667–675

71. Zhang J, Sun P, Jiang P, Guo Z, Liu W, Lu Q, Cao W (2019) Formation mechanism of TiO_2 polymorphs under hydrothermal conditions based on structure evolution of $[Ti(OH)_h(H_2O)_{6-h}]_{4-h}$ monomers. J Mater Chem C 7:5764–5771

72. Draman SFS, Daik R, Latif FA, El-Sheikh SM (2014) Characterization and thermal decomposition kinetics of kapok (*Ceiba pentandra* L.)-based cellulose. BioResources 9(1):8–23

73. Cao Y, Xie L, Sun G, Su F, Kong QQ, Li F, Ma W, Shi J, Jian D, Lu C, Chen CM (2018) Hollow carbon microtubes from kapok fiber: structural evolution and energy storage performance. Sustain Energy Fuels 2:455–465

74. Islam MS, Miran MS, Rahman MM, Mollah MYA, Susan MABH (2013) Polyaniline-silica composite materials: influence of silica content on the thermal and thermodynamic properties. J Nanostruct Polym Nanocompos 9(3):84–90

75. Zhang L, Liu P, Su Z (2006) Preparation of PANI-TiO$_2$ nanocomposites and their solid-phase photocatalytic degradation. Polym Degrad Stabil 91:2213–2219

76. Hubbe MA, Azizian S, Douben S (2019) Implication of apparent-second-order adsorption kinetics onto cellulosic materials: a review. BioResources 14(3):7582–7626

77. Hidalgo D, Bocchini S, Fontana M, Saracco G, Hernandez S (2015) Green and low-cost synthesis of PANI-TiO$_2$ nanocomposite mesoporous films for photoelectrochemical water splitting. R Soc Chem Adv 5:49429–49438

78. Lin Y, Li D, Hu J, Xiao G, Wang J, Li W, Fu X (2012) Highly efficient photocatalytic degradation of organic pollutants by PANI-modified TiO$_2$ composite. J Phys Chem C 116:5764–5772

79. Dai K, Chen H, Peng T, Ke D, Yi H (2007) Photocatalytic degradation of methyl orange in aqueous suspension of mesoporous titania nanoparticles. Chemosphere 69:1361–1367

80. Baiocchi C, Brussino MC, Pramauro E, Bianco Prevot A, Palmisano L, Marci G (2002) Characterization of methyl orange and its photocatalytic degradation products by HPLC/UV-VIS diode array and atmospheric pressure ionization quadrupole ion trap mass spectrometry. Int J Mass Spectro 214:247–256

81. Bianco Prevot A, Basso A, Baiocchi C, Pazzi M, Marci G, Augugliario V, Palmisano L, Pramauro E (2004) Analytical control of photocatalytic treatments: degradation of sulfonated azo dye. Anal Bioanal Chem 378:214–220

82. Aarthi T, Madras G (2008) Photocatalytic reduction of metals in presence of combustion synthesized nano-TiO$_2$. Catal Commun 9:630–634

83. Chen D, Ray AK (2001) Removal of toxic metal ions from wastewater by semiconductor photocatalysis. Chem Eng Sci 56:1561–1570

84. Testa JJ, Grela MA, Litter MI (2004) Heterogeneous photocatalytic reduction of chromium(VI) over TiO$_2$ particles in the presence of oxalate: involvement of Cr(V) species. Environ Sci Technol 38:1589–1594

85. Murruni L, Leyva G, Litter M (2007) Photocatalytic removal of Pb(II) over TiO$_2$ and Pt-TiO$_2$ powders. Catal Today 129:127–135

86. Li L, Jiang F, Liu J, Wan H, Wan Y, Zheng S (2012) Enhanced photocatalytic reduction of aqueous Pb(II) over Ag loaded TiO$_2$ with formic acid as hole scavenger. J Environ Sci Health A Toxic Hazard Subst Environ Eng 47(3):327–336

87. Zimbone M, Buccheri MA, Cacciato G, Sanz R, Rappazzo G, Boninelli S, Reitano R, Romano L, Privitera V, Grimaldi MG (2015) Photocatalytical and antibacterial activity of TiO$_2$ nanoparticles obtained by laser ablation in water. Appl Catal B Environ 165:487–494

88. Wen B, Waterhouse GIN, Jia MY, Jiang ZH, Zhang ZM, Yu LM (2019) The feasibility of polyaniline-TiO$_2$ coatings for photocathodic antifouling: antibacterial effect. Synth Metals 257:116175

89. Liu IF, Annamalai T, Sutherland JH, Tse-Dinh YC (2009) Hydroxyl radicals are involved in cell killing by bacterial topoisomerase I cleavage complex. J Bacteriol 191(16):5315–5319

90. Muñoz-Bonilla A, Fernández-García M (2015) The roadmap of antimicrobial polymeric materials in macromolecular nanotechnology. Eur Polym J. https://doi.org/10.1016/j.eurpolymj.2015.01.030